JGR Solid Earth

RESEARCH ARTICLE
10.1029/2020JB020122

Permeability Variations in Illite-Bearing Sandstone: Effects of Temperature and NaCl Fluid Salinity

Chaojie Cheng[1,2] and **Harald Milsch**[1]

[1]Section 4.8 - Geoenergy, GFZ German Research Centre for Geosciences, Potsdam, Germany, [2]Institute for Geosciences, University of Potsdam, Potsdam, Germany

Key Points:
- Flow-through experiments were conducted to investigate permeability variations in illite-bearing sandstone upon heating and fluid exchanges
- Heating results in irreversible permeability impairment caused by thermo-mechanical pore throat closure irrespective of fluid composition
- Subsequent pore fluid dilution yields additional permeability damage resulting from illite mobilization in agreement with DLVO theory

Supporting Information:
- Supporting Information S1

Correspondence to:
H. Milsch,
milsch@gfz-potsdam.de

Citation:
Cheng, C., & Milsch, H. (2020). Permeability variations in illite-bearing sandstone: Effects of temperature and NaCl fluid salinity. *Journal of Geophysical Research: Solid Earth*, *125*, e2020JB020122. https://doi.org/10.1029/2020JB020122

Received 3 MAY 2020
Accepted 28 AUG 2020
Accepted article online 7 SEP 2020

Abstract Temperature changes and variations in pore fluid salinity may negatively affect the permeability of clay-bearing sandstones with implications for natural fluid flow and geotechnical applications alike. In this study these factors are investigated for a sandstone dominated by illite as the clay phase. Systematic long-term flow-through experiments were conducted and complemented with comprehensive microstructural investigations and the application of Derjaguin-Landau-Verwey-Overbeek (DLVO) theory to explain mechanistically the observed permeability changes. Initially, sample permeability was not affected by low pore fluid salinity indicating strong attraction of the illite particles to the pore walls as supported by electron microprobe analysis (EMPA). Increasing temperature up to 145°C resulted in an irreversible permeability decrease by 1.5 orders of magnitude regardless of the pore fluid composition (i.e., deionized water and 2 M NaCl solution). Subsequently diluting the high salinity pore fluid to below 0.5 M yielded an additional permeability decline by 1.5 orders of magnitude, both at 145°C and after cooling to room temperature. By applying scanning electron microscopy (SEM) and mercury intrusion porosimetry (MIP) thermo-mechanical pore throat closure and illite particle migration were identified as independently operating mechanisms responsible for observed permeability changes during heating and dilution, respectively. These observations indicate that permeability of illite-bearing sandstones will be impaired by heating and exposure to low salinity pore fluids. In addition, chemically induced permeability variations proved to be path dependent with respect to the applied succession of fluid salinity changes.

1. Introduction

When the thermal and/or chemical equilibrium in geological formations is disturbed by variations in environmental conditions, permeability changes may occur. Understanding the mechanistic origin of these changes in geological porous media is crucial to reconstructions and predictions of natural fluid flow within the Earth's crust, as well as hydraulic properties in geotechnical applications, hydrocarbon (petroleum and gas) exploitation, CO_2 sequestration, nuclear waste disposal, and geothermal reservoir utilization (e.g., Huenges, 2010; Juanes et al., 2006; Sundberg et al., 2009). As an example, seasonal heat storage in geothermal aquifers and exploitation of geothermal reservoirs affect the temperature gradient within the formation. Fluid composition may also significantly change in the course of producing and/or injecting fluids from/into a reservoir.

Thermally induced permeability variations were previously investigated in various sedimentary rocks. Contrary to intuition, it is commonly observed that a thermal expansion of the solid matrix leads to a pore volume decrease and, consequently, a permeability reduction in intact rocks (Casse & Ramey, 1979; Gräf et al., 2013; Somerton, 1980, 1992; Somerton et al., 1981), given that the microstructure of a polycrystalline rock is heterogeneous in nature. In contrast, anisotropic thermal expansion might result in thermal cracks (Wong & Brace, 1979), which may enhance permeability. A number of experimental studies performed on Berea, Vosges, Upper Coal, and Fontainebleau sandstones indicate that increasing temperature causes a permeability decrease that in most cases is fully or at least partially recovered after cooling (e.g., Jing, 1990; McKay & Brigham, 1984; Rosenbrand et al., 2015; Sun et al., 2016). In some cases, recovered permeability can be slightly higher than the initial one (Baudracco & Aoubouazza, 1995). In contrast, the permeability of some low-permeable sandstones was observed to be independent of temperature (Gobran et al., 1987; Potter et al., 1980; Wei et al., 1986). The permeability of Berea sandstone to oil increased

Table 1
Mineral Composition of Flechtinger Sandstone From X-ray Powder Diffraction

Minerals	Content (wt%)
Quartz	60.6
Calcite	3.0
K-feldspar	12.8
Albite	13.3
Illite	9.9
Hematite	0.4

slightly with temperature in contrast to its permeability to water, which decreases, and to gas, which is independent of temperature (Casse & Ramey, 1979).

Chemically induced permeability changes in clay-bearing sandstones related to low-salinity fluids are well-known (e.g., Azari & Leimkuhler, 1990; Khilar & Fogler, 1984; Kia et al., 1987; Mohan et al., 1993; Mohan & Fogler, 1997; Mungan, 1968; Omar, 1990; Rahman et al., 1995; Sharma et al., 1985; Yu et al., 2018). Generally, permeability is not reduced unless the salinity is lower than a critical salt concentration (CSC). In this case, the release and dispersion of clay aggregates are triggered, clogging pore throats. The CSC depends strongly on the cation type within the aqueous solution. K^+-saturated clay-bearing sandstones show a significantly lower CSC as compared to that of Na^+-saturated sandstones (e.g., Azari & Leimkuhler, 1990). Bivalent cations like Ca^{2+} and Mg^{2+} stabilize permeability down to very low salt concentrations (Gray, 1966; Khilar & Fogler, 1984; Mohan et al., 1993; Mungan, 1968). Derjaguin-Landau-Verwey-Overbeek (DLVO) theory (Deraguin & Landau, 1941; Verwey, 1947; Appendix A) is often applied to account for clay particle release (e.g., Bhattacharjee et al., 1998; Tchistiakov, 2000), but other types of theoretical models, incorporating hydrodynamic interactions, were also derived in this regard (e.g., Bedrikovetsky et al., 2011, 2012; Russell et al., 2018). Overall, clay particle release will occur when hydrodynamic forces and physico-chemical repulsion dominate over any process yielding attraction of the particles toward the pore walls (e.g., Tchistiakov, 2000).

Whether or not a clay-bearing sandstone shows permeability variations upon changes in thermo-chemical conditions is strongly dependent on clay type (Wilson et al., 2014). In previous theoretical and experimental studies, sandstones containing predominantly kaolinite received particular attention in this regard (e.g., Khilar & Fogler, 1983; Musharova et al., 2012; Rosenbrand et al., 2015; Schembre & Kovscek, 2005; You et al., 2016). Here, for experiments, Berea sandstone has become a reference material. In contrast, experimental investigations on sandstones containing illite as the dominant clay phase are scarce in this context. This particularly concerns studies that were conducted at multiple temperatures and in combination with salinity changes.

In this study, we conducted comprehensive long-term experiments to systematically investigate changes in rock permeability upon thermo-chemical forcing. Flow-through experiments on illite-bearing sandstone samples were complemented with extensive comparative microstructural investigations to explain the observations mechanistically. In section 2 details of the experimental and analytical methodologies are given. Section 3 reports the permeability and microstructural results which are integrated and discussed in section 4.

2. Experimental and Analytical Methodologies

2.1. Sample Material

Flechtinger sandstone, a Lower Permian (Upper Rotliegend) sedimentary rock outcropping and commercially mined at the Sventesius quarry near Flechtingen, Germany, was selected for the experiments. Table 1 lists the mineralogical composition of the material measured by X-ray powder diffraction (XRD) indicating that illite is the dominant clay phase in this rock having a content of approximately 10% by weight. Other clay types, for example, mixed-layer clays, were only found in trace amounts.

Four cylindrical cores were drilled from a larger block. The sample material is homogenous in macroscopic appearance but shows bedding as a result of sedimentation. In order to reduce any effect of texture and anisotropy during the flow-through experiments, all samples were cored perpendicular to the bedding. Subsequently, samples were prepared with polished and plane-parallel end faces having a diameter of 30 mm and a length of 40 mm. The four samples were labeled S2, FS1, FS3, and FS4, respectively. Sample S2 was later used as the reference (starting) material to compare microstructural changes that had occurred during the flow-through experiments conducted with samples FS1, FS3, and FS4.

Samples FS1, FS3, and FS4 were vacuum-dried in an oven at 60°C for 24 hr. They were then set under vacuum in a desiccator chamber for 10 hr and saturated with deionized water for another 24 hr. Dry mass

and saturated mass were measured to calculate the initial (connected) porosities yielding 9.2% for sample S2, 9.0% for FS1, 9.7% for FS3, and 10.9% for FS4, respectively. After the experiments, the samples were vacuum-dried again, in order to detect any potential dry mass loss.

2.2. Flow-Through Apparatus and Sample Assembly

All experiments were performed with two flow-through apparatuses with details described in Milsch et al. (2008). Wetted parts in one of the devices are made of Hastelloy C-276 for experiments with saline fluids. Oil-medium based confining pressure is generated with one ISCO 65D syringe pump. The pore fluid system consists of two ISCO 260D syringe pumps, one upstream and one downstream, to apply pore pressure and to realize flow. The flow rate can be as low as 0.001 ml/min.

Heating of the oil inside the pressure vessel is performed with a hollow-cylindrical resistance heater capable of 200°C. Two Pt100-type Resistance Temperature Detectors (RTD) within the pressure vessel are closely attached to the rock sample to monitor temperature. All pumps and their controllers are connected to a computer program that permits data acquisition.

The saturated sample is jacketed with a Fluorinated Ethylene Propylene (FEP) heat shrink tubing and is then mounted in the vessel. Afterward, the two sample ends are connected to the upstream and downstream pumps, respectively. The flow direction, generally, is from the bottom to the top side of the sample but can be reversed for return permeability measurements. The upstream capillary forms a spiral around the sample within the oil bath of the pressure vessel permitting the injecting fluid to heat up before entering the sample.

2.3. Flow-Through Experiments

Intermittent flow-through experiments were carried out at constant temperature and pressure conditions. Permeability k was measured applying steady-state flow and was calculated using Darcy's law (Brown, 2002; Darcy, 1856) directly. Q is the volumetric flow rate through the sample, A is the cross-sectional area, Δp is the differential pressure over the sample length L, and μ the dynamic fluid viscosity is adjusted depending on fluid type, salinity, temperature, and pore pressure:

$$k = \frac{Q\mu L}{\Delta p A} \tag{1}$$

Due to the temperature difference in the pump cylinders and the pressure vessel, the flow rate Q through the sample was corrected in accordance with the pump flow rate Q_p and the fluid densities ρ_p at room temperature and ρ_v at vessel temperature, respectively:

$$Q = \frac{Q_p \rho_p}{\rho_v} \tag{2}$$

Pore pressure was maintained constant at 1 MPa and thus was high enough to prevent fluid boiling at the maximum experimental temperature, that is, 145°C (Guildner et al., 1976). During the permeability measurements the downstream pump was operated in constant pressure mode at 1 MPa, and the upstream pump was maintained in constant flow rate mode. In dependence on sample permeability the flow rate was varied to keep the pressure difference between the sample ends below 0.5 MPa to minimize the distortion of the effective stress state. As was observed, a permeability decrease could occur rapidly. Hence, flow rate had to be adjusted timely to ensure that the upstream pressure would be limited to 1.5 MPa at steady state. Confining pressure was held constant at 10 MPa throughout the experiments.

Temperature was increased and decreased stepwise by intervals of approximately 20°C between room temperature and 145°C. An (active) temperature increase by 20°C took about 4 hr and (passive) cooling by 20°C required up to 24 hr to ensure that the respective target temperature was homogeneously distributed throughout the sample.

In addition to deionized water, three different NaCl solutions were used as the pore fluid with concentrations of 0.5, 1.0, and 2.0 M, respectively, exchanging pore fluid. Densities and dynamic viscosities of the fluids were adjusted for the respective temperatures and pressures (Cooper, 2008; Joseph et al., 1981). At the initiation of

Table 2
Summary of Experimental Conditions

Sample	Permeating fluids	Temperature steps (°C)	Flow rate range (ml/min)
FS1	H_2O	25 ↔ 40 ↔ 60 ↔ 80 ↔ 100 ↔ 120 ↔ 141	0.05–2.00
FS3	H_2O → 2 M Na → 1 M Na → 0.5 M Na → H_2O	25 ↔ 40 ↔ 60 ↔ 80 ↔ 100 ↔ 120 ↔ 145	0.02–2.00
FS4	H_2O → 2 M Na → 1 M Na → 0.5 M Na → H_2O	27 ↔ 40 ↔ 60 ↔ 81 ↔ 100 ↔ 122 ↔ 145	0.005–2.00

Note. H_2O, 2 M Na, 1 M Na, and 0.5 M Na are deionized water, 2.0 M NaCl, 1.0 M NaCl, and 0.5 M NaCl solutions, respectively. The electrical conductivity of deionized water was approximately 20 μS/cm at 25°C.

experiments and during initial sample saturation (section 2.1), the pump cylinders and capillaries were filled with deionized water. Fluid exchanges were performed by emptying the upstream pump cylinder and refilling it with the next fluid of choice. The volume of the upstream capillary connected to the sample is approximately 3 ml. Therefore, care had to be taken that the total fluid volume that flowed through the sample was always large enough to ensure that the previous pore fluid was exchanged completely by the new fluid. For all experiments, the final fluid that was flushed through a sample, again, was deionized water to ensure that no salt precipitation would occur upon drying the samples in preparation for the microstructural analyses. The total duration of the experiments with samples FS1, FS3, and FS4 was 54, 44, and 40 days, respectively.

It should be noted at this point that for none of the experiments there was an indication of oil intrusion from the confining pressure into the pore fluid system. Any related experimental artifact yielding (apparent) changes in permeability, therefore, can be excluded.

Table 2 shows the order of the permeating fluids used, the temperature steps, and the flow rate range of each experiment. Sample FS4 underwent further experimental steps after those shown in Table 2 which are beyond the scope of the present study. This likely overprinted the microstructure of this sample. For this reason, our evaluations of microstructural changes associated with experimental measurements are made for samples FS1 and FS3 as outlined in section 2.4.

Overall, the purpose of the experimental strategy was to investigate (a) the effect of a temperature increase for isochemical fluid conditions in terms of permeability changes and their potential reversibility as a result of a temperature decrease and return flow, respectively (sample FS1), (b) the potential hydrodynamic mobilization of fines (sample FS3), and (c) the effect of a decrease in NaCl pore fluid salinity at two different temperatures (samples FS3 and FS4).

2.4. Microstructural Analyses

Samples S2, FS1, and FS3 were examined to evidence and compare microstructural changes in the course of the flow-through experiments. Figure 1 shows the individual parts of the samples as used for the different analyses. For each sample, polished thin sections and saw-cut thick sections, taken parallel and perpendicular to the flow direction, were prepared and carbon coated. Scanning electron microscopy (SEM) was used for qualitative imaging of illite and pore space microstructure in SE and BSE modes, respectively. Electron microprobe analysis (EMPA) was applied on the thin sections to quantitatively detect element content variations in illite. Two subsamples along the flow direction were prepared for mercury intrusion porosimetry (MIP) to investigate porosity differences and changes in pore-size distribution.

In MIP, the pore diameter D is related to the capillary pressure P_c based on the Washburn (1921) equation:

$$D = -\frac{4\gamma\cos(\theta)}{P_c} \tag{3}$$

where $\gamma = 0.48$ N/m is the surface tension and $\theta = 140°$ is the contact angle of mercury. The fraction of sample porosity for each pressure step during a measurement is expressed as $\phi_{Hg,i} = dV_{Hg}/V_s$, where dV_{Hg} is the incremental volume of the injected mercury and V_s is the sample bulk volume. Finally, the cumulative (total connected) porosity is calculated as

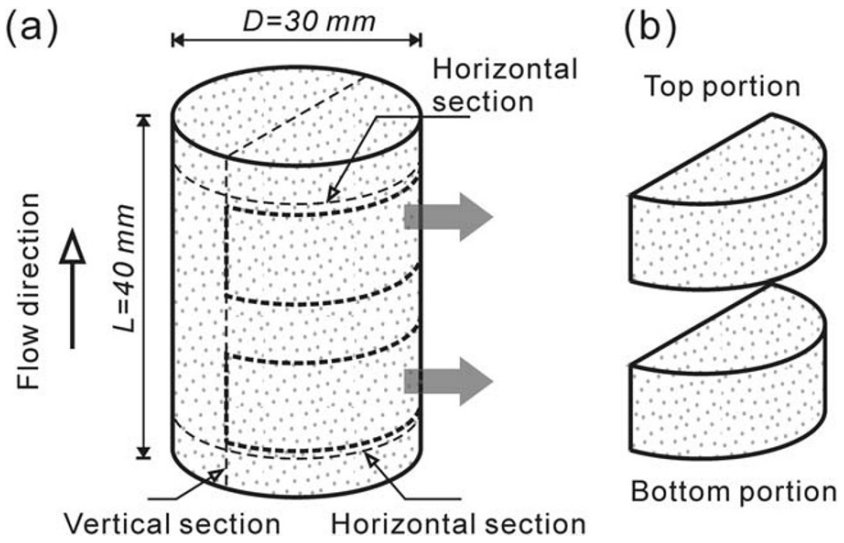

Figure 1. Schematic sketch of sample preparation for the different microstructural analyses. (a) Cylindrical core sample and locations of thin and thick sections prepared for scanning electron microscopy (SEM) and electron microprobe analysis (EMPA); (b) top and bottom portions of the samples used for mercury intrusion porosimetry (MIP).

$$\phi_{MIP} = \sum \phi_{Hg,\,i} \tag{4}$$

The resulting porosity of sample S2 was 9.4%, which is in reasonable agreement with the value obtained from saturation and weighing (section 2.1).

2.5. Initial Rock Microstructure

Figure 2 shows micrographs of the starting material (sample S2) at different magnifications. Figures 2a and 2b were taken on the polished thin sections in BSE mode. Pores and pore throats, as those shown in Figure 2a, represent the typical flow paths. Pores and pore throats are partially filled with illite and, occasionally, some fines. The widths of pore throats are significantly smaller than those of the pores. Figure 2b shows that illite can occur as aggregates with both open and compact appearance. Within the pores and pore throats, illite develops three structural types: tangential illite, pore-lining illite, and pore-filling illite, respectively (Desbois et al., 2016; Wilson et al., 2014). The compact tangential illite has variable thickness and is directly attached to the grain walls. The pore-lining illite is either connected to the tangential illite or directly to the grain walls. The pore-filling illite, with both fibrous and platy morphologies, appears to be mostly unconnected but can link to other illite types or the grain walls. Overall, these three types of illite are not uniformly distributed within the pores and pore throats. Moreover, they play a dominant role in defining the rock's transport properties.

Figures 2c–2f, taken on saw-cut thick sections in SE mode, display images of the different illite types within the pore space. The pore-lining illite shown in Figure 2c is located in a pore throat and stretches toward the pore space, while its other end is tightly bound to tangential illite. Figure 2d presents an example of pore-filling illite in a pore throat. In this case, the platy illite crystals form aggregates and partially clog the pore throat. Flocculent fibrous illite, as shown in Figure 2e, is found occasionally within the pore space and is classified here as pore-lining illite. All grain walls were found to be coated with tangential and/or pore-lining illite (Figure 2f), and both illite types are authigenic (Desbois et al., 2016; Wilkinson & Haszeldine, 2002; Wilson et al., 2014).

3. Results

3.1. Flow-Through Experiments and Permeability

Figure 3 displays the permeability evolution of each sample (FS1 in (a), FS3 in (b), and FS4 in (c)) as a function of temperature during the total progress of each experiment. All individual permeability values (dots) as

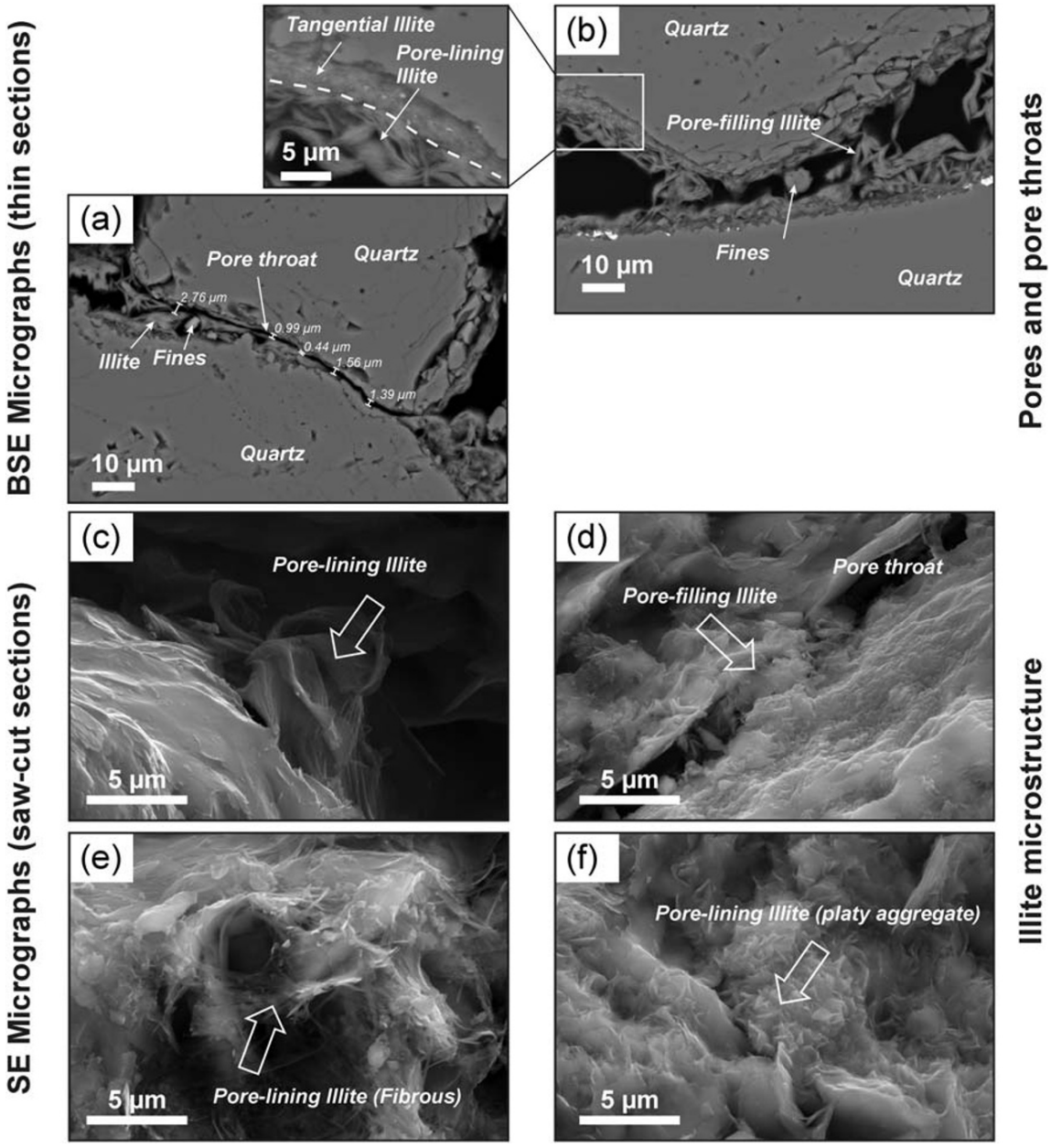

Figure 2. Scanning electron micrographs in BSE and SE modes of the starting material (sample S2) at different magnifications. (a) Representative microstructure of pores and pore throats in Flechtinger sandstone; (b) structural types of illite found in the pore space (tangential, pore-lining, and pore-filling); (c) pore-lining illite bound to tangential illite; (d) platy pore-filling illite within a pore throat; (e) fibrous pore-lining illite within a pore; (f) tangential and platy pore-lining illite covering the pore walls.

well as details of other experimental parameters are provided in Appendix B and in Cheng and Milsch (2020). To recall, all experiments started with deionized water as the pore fluid.

For sample FS1 (Figure 3a), when heating the sample from 25 to 80°C, permeability decreased by approximately 1.5 orders of magnitude from 5.0 to 0.2 mD (1 mD = 0.987×10^{-15} m^2) with no further significant changes up to 141°C. Subsequent cooling to 41°C did not yield permeability recovery. A subsequent (second) heating-cooling cycle had a negligible effect on permeability. Finally, reversing the flow direction did not affect permeability which thus did not recover as a result of return flow. In summary, once temperature increases beyond approximately 80°C, the permeability of this rock decreases significantly and irreversibly when deionized water is used as the pore fluid with (almost) no more changes observed afterward.

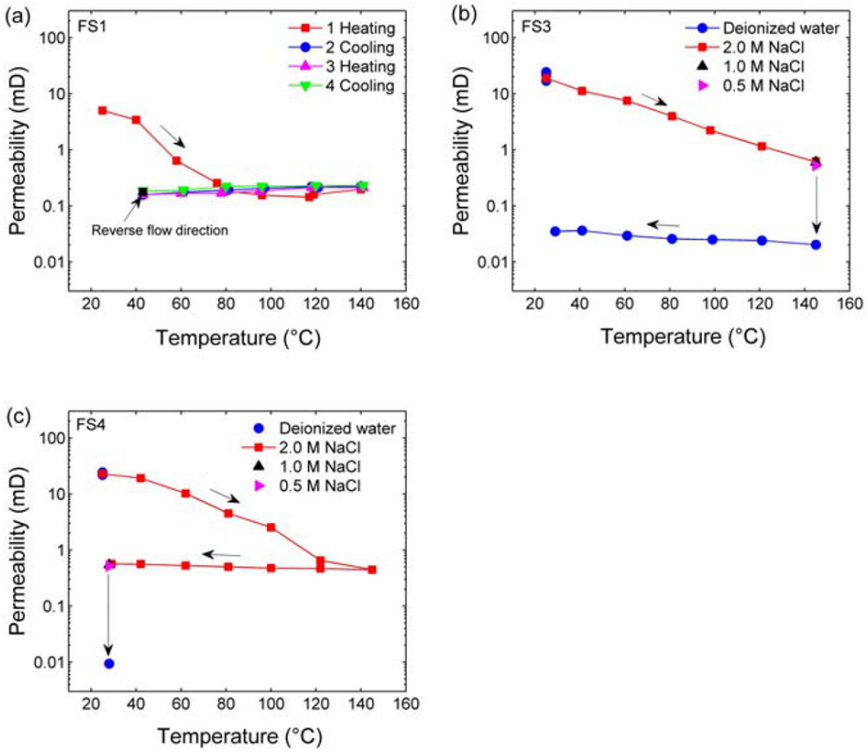

Figure 3. Permeability as a function of temperature for samples FS1 (a), FS3 (b), and FS4 (c). Each dot is a steady-state permeability measurement at some constant temperature level and at constant confining and pore pressures, respectively. Systematic successions of temperature and salinity changes were implemented with implications for permeability summarized in this figure and detailed in section 3.1.

For sample FS3 (Figure 3b), to investigate a possible effect of fine particle migration on permeability due to hydrodynamic interactions and before any temperature or salinity changes, more than 1,100 ml of deionized water was injected into the sample at a flow rate of 2.0 or 1.0 ml/min. Permeability first decreased from 25.2 to 17.0 mD and then remained constant until the end of this experimental stage. Subsequently, the pore fluid was exchanged by a 2.0 M NaCl solution, after which permeability recovered to 19.0 mD. The following temperature increase from 25 to 145°C caused permeability to decrease log-linearly, again by approximately 1.5 orders of magnitude, from 19.0 to 0.6 mD. At 145°C, pore fluid salinity was reduced stepwise to 1.0 and 0.5 M NaCl with only a marginal effect on permeability (0.6 to 0.5 mD). In contrast, when deionized water was reintroduced, permeability decreased significantly from 0.5 to 0.02 mD. Cooling to room temperature only yielded a negligible permeability increase from 0.02 to 0.04 mD. Total permeability reduction thus spanned over three orders of magnitude. In summary, hydrodynamically induced fine particle migration in this rock is negligible for the present flow rate range and as long as no thermo-chemical alteration of the illite and pore space microstructure has been induced. Permeability is reduced at temperature increases also for high NaCl salinity pore fluids. A further decrease in permeability is observed when deionized water is reintroduced at high temperature. The permeability is reduced after a successive temperature increase-salinity decrease sequence is (nearly) irreversible when temperature is decreased again.

Sample FS4 (Figure 3c) experienced a similar series of steps as imposed on sample FS3, the key difference is that temperature was decreased before the salinity decrease which then was performed at room temperature. Firstly, after a flow of 32 ml of deionized water, permeability had decreased slightly from 24.3 to 21.8 mD. The pore fluid was then replaced by a 2.0 M NaCl solution after which permeability had slightly recovered to 22.8 mD. Subsequent heating from 27 to 145°C led to a permeability decrease from 22.8 to 0.5 mD after which cooling to 28°C, again, yielded virtually no permeability recovery. At 28°C salinity was decreased by successive fluid exchanges (1.0 M NaCl, 0.5 M NaCl, and deionized water) with the same effects as those observed

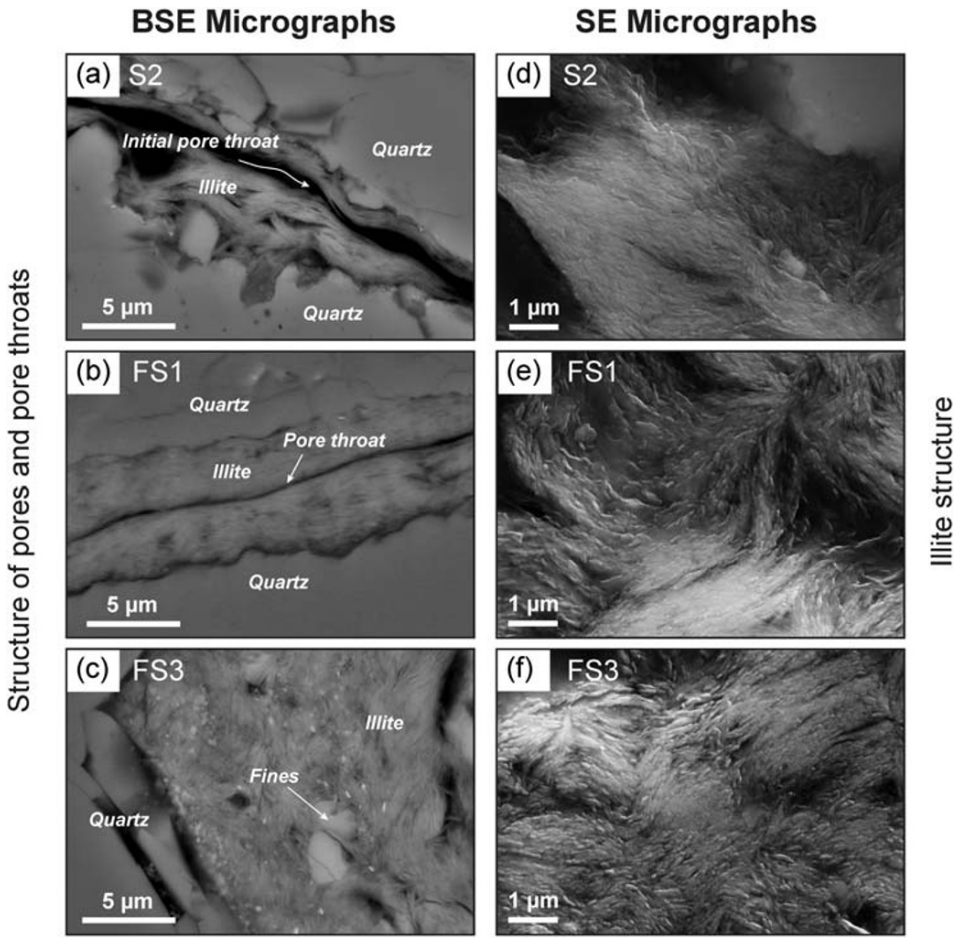

Figure 4. Comparison of the microstructure of the samples before and after the flow-through experiments. Scanning electron microscope (SEM) images of the vertical polished thin and saw-cut thick sections, respectively (Figure 1). BSE mode images taken of the thin sections show: (a) open pore throats in the starting material (sample S2); (b) closed pore throat after temperature cycling only (sample FS1); (c) closed pore throat after the temperature cycle and the fluid exchanges (sample FS3). SE mode images taken of the thick sections might indicate changes in illite morphology, comparing images of (d) starting material (sample S2) and flow-through experimental samples (e) FS1 and (f) FS3 (see section 3.2).

for sample FS3. The final permeability of sample FS4 was 0.01 mD. In summary, the observations reported before for sample FS3 are reproducible for identical procedural steps and possess an excellent quantitative comparability. The previously observed permeability decrease as temperature is increased for high NaCl salinity pore fluid conditions is also irreversible when temperature is directly decreased. Finally, a severe and further permeability reduction is observed upon a salinity decrease at low temperatures.

3.2. Microstructural Evolution

The SEM micrographs in Figure 4 of both the starting material (sample S2) and the samples after the flow-through experiments (FS1 and FS3) show changes in pore throat and illite microstructures. For imaging of the pore throats (Figures 4a–4c), the micrographs were taken in BSE mode on the polished thin sections. The walls of pore throats, like the one shown in Figure 4a (sample S2), are completely lined with illite significantly reducing the original grain-to-grain distance and resulting in narrow but open flow channels. In contrast, the pore throat in Figure 4b (sample FS1) is virtually closed after the applied heating and cooling cycles. The same is true for the pore throat in Figure 4c (sample FS3) after the succession of temperature cycling and fluid exchanges. In comparison to sample FS1, the appearance of the pore throat filling in sample FS3 suggests that the illite particles not only were compacted but also experienced some amount of

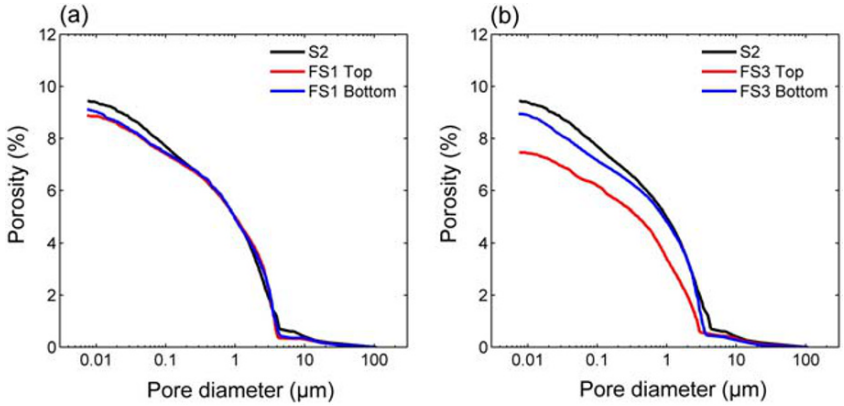

Figure 5. Cumulative porosity as a function of pore diameter measured by mercury intrusion porosimetry (MIP). (a) Sample FS1 in comparison to the starting material (sample S2) with results for the bottom and top portions (Figure 1) indicated in blue and red, respectively. (b) Sample FS3 in comparison to sample S2. Overall, contrasting changes in pore-size distribution are evident that relate to the effects of temperature cycles (FS1) and the additional fluid exchanges (FS3) as outlined in section 3.2.

displacement yielding illite particle pile-ups. Nominally closed pore throats were also found in sample S2. However, they appear at a significantly larger number in samples FS1 and FS3.

For imaging of the illite microstructure (Figures 4d–4f), the micrographs were taken in SE mode on the saw-cut thick sections. Overall, at the μm-scale, morphological changes were hard to detect, and possibilities of definite statements are very limited. However, the wider surface of the platy pore-lining illite aggregates in the starting material (sample S2; Figure 4d) appears slightly smoother than observed in Figure 4e (sample FS1) or Figure 4f (sample FS3). Here, the images suggest some small degree of surface roughening and clay platelet loosening that might have resulted from heating (sample FS1) and, additionally, from the fluid exchanges (sample FS3).

Figure 5 shows the pore-size distribution in samples FS1 (Figure 5a) and FS3 (Figure 5b) after the flow-through experiments compared to the starting material (sample S2) as obtained from mercury intrusion porosimetry (MIP) and evaluated according to Equations 3 and 4. Weight measurements (section 2.1) indicate that the dry mass loss of the samples associated with fluid flow is very small, in the range of 30 mg (FS1) to 100 mg (FS3). This indicates that nearly all material that could potentially be mobilized (i.e., approximately 6.7 g of illite) is still contained within the respective sample.

For sample FS1 (Figure 5a), the cumulative (total connected) porosity curves of the bottom and the top portions (Figure 1) are virtually identical, indicating a very similar pore-size distribution after the experiment. However, compared to the starting material (sample S2), the cumulative porosity of both subsamples decreased slightly in the course of the experiment, that is, by approximately 0.4% porosity. In connection with the evolution of permeability (section 3.1) these observations strongly suggest that (1) the hydraulic properties of the starting material are governed by pores and pore throat sizes of 0.2 μm and below, (2) temperature cycling resulted in partial and irreversible pore throat closure predominantly in this pore-size range, and (3) there was no displacement of solid material from the bottom to the top of the sample as fluid flowed.

For sample FS3 (Figure 5b), there is a significant mismatch in the pore-size distributions of the top and bottom portions of the sample. The overall decrease in cumulative porosity is large, particularly in the top portion where porosity is reduced by 1.9%. The fraction of pores affected most by the microstructural changes has increased to pore sizes of approximately 1 μm in the bottom portion and 3 μm in the top portion of the samples. The additional decrease in sample permeability as a result of the fluid exchanges is mirrored by these structural alterations of the pore space. Moreover, the mismatch in the pore-size distributions of the two subsamples suggests displacement of material in the direction of flow that progressively piles up yielding additional pore throat closure over an extended pore size range.

Table 3
Median Concentrations of Na, K, Ca, and Mg Oxides in Pore-Filling Illite Before and After the Flow-Through Experiments

Sample/section	Na_2O (wt%)	K_2O (wt%)	CaO (wt%)	MgO (wt%)	No. of locations
S2	0.03	7.65	0.28	1.25	16
FS1	0.06	7.91	0.35	0.98	16
FS3_1	0.19	7.24	0.35	1.09	17
FS3_2	0.14	8.12	0.43	1.03	14

Note. The values for S2 and FS1 relate to the respective vertical thin sections (Figure 1). The designations FS3_1 and FS3_2 denote measurements taken on the vertical and the bottom thin sections of this sample, respectively.

It should be noted that the use of sample S2 as the starting material reference may yield a small uncertainty in the comparison of total porosities in the order of 0.2%. This, however, does only marginally affect the reasoning that a reduction in the contribution of the smaller pore size fractions to total porosity yields the observed permeability changes in FS1 and FS3. This is supported by the fact that both the S2 and FS1 porosity-pore size curves are, otherwise, absolutely identical in their characteristics up to the inflection point at around 4 μm (Figure 5a).

Pore-filling illite was further investigated using electron microprobe analysis (EMPA; at 8 kV and 1.2 nA with 5 μm probe size) on polished thin sections of samples S2, FS1, and FS3. Element concentrations of Na, K, Si, Al, Ca, and Mg were measured. Fe was not detected. In the following, we focus attention on concentrations of Na^+, K^+, Ca^{2+}, and Mg^{2+} given that these are the exchangeable cations of illite. Table 3 lists the measured (median) concentrations of the respective oxides within the different samples. For each thin section, measurements were performed at 14 to 17 locations.

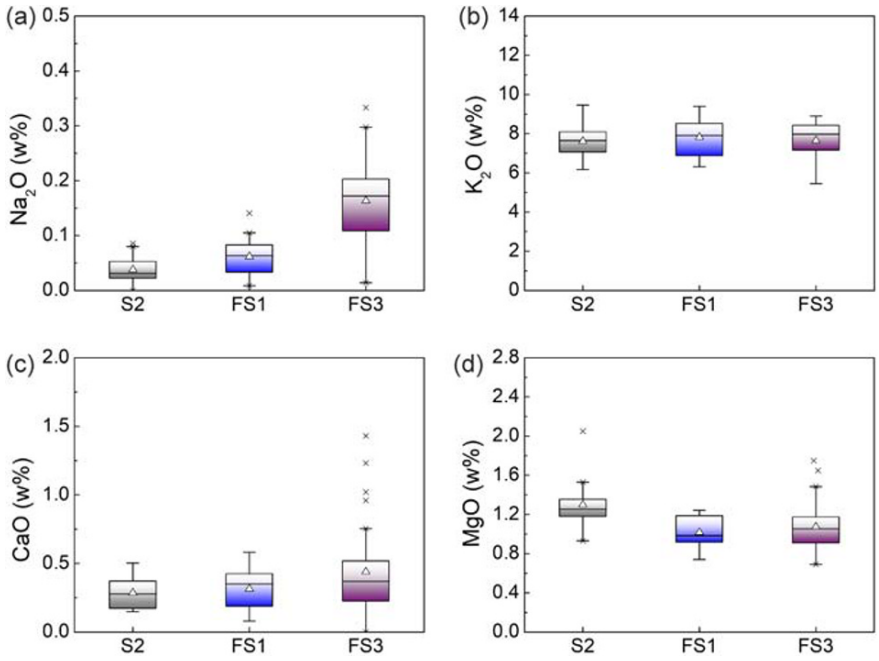

Figure 6. Concentrations of Na (a), K (b), Ca (c), and Mg (d) oxides in pore-filling illite before (sample S2) and after (samples FS1 and FS3) the flow-through experiments as measured by electron microprobe analysis (EMPA) on polished thin sections. The solid line and the open triangle in the respective box indicate the median and mean of each data set, respectively. Individual symbols (x) above and below the error bars are measured data but statistical outliers. In the box plots, the boxes signify the lower and upper quartiles, Q1 and Q3, of the data sets, respectively. The upper and lower horizontal error bar lines indicate the largest and smallest data values for Q3 + 1.5 IQR and Q1–1.5 IQR, respectively, where IQR is the interquartile range equal to Q3–Q1. Overall, significant changes in ionic elemental concentration are only evident for Na^+ in sample FS3 as outlined in section 3.2.

Figure 6 presents box plots of Na (a), K (b), Ca (c), and Mg (d) oxide concentrations in pore-filling illite for the different samples (S2, FS1, and FS3), respectively. In all samples, K^+ is evidently the most abundant exchangeable cation in this illite. Conversion of the median concentrations from wt% to mol/g was then performed by applying $2\omega/(M\,z)$, where ω and M are the weight percent concentration and molecular weight of the respective oxide, and z is the valence of the corresponding cation, respectively. This yields that the pore-filling illite within the starting material (sample S2) contains 0.01 mmol/g Na^+, 1.62 mmol/g K^+, 0.05 mmol/g Ca^{2+}, and 0.31 mmol/g Mg^{2+}, respectively. It should be noted that Mg^{2+}, in addition to the exchangeable sites in the interlayer, can also be located in the octahedral layer (Anderson et al., 2010). Compared to the starting material, the relative changes of K^+, Ca^{2+}, and Mg^{2+} in both samples FS1 and FS3 are negligible. This is also true for Na^+ in FS1. In sample FS3, however, there is a substantial increase in Na^+ content that corresponds to the long-term exposure of the illite contained in this sample to NaCl solutions of high salinity during the experiment. Overall, the EMPA analyses yield for FS3 and yield the maximum Na^+ content in pore-filling illite after the experiment was 0.11 mmol/g with a median of 0.05 mmol/g. From this result one can infer that the cation exchange capacity (*CEC*) of this illite is no more than approximately 0.11 mmol/g. Both maximum and median Na^+ concentrations will later be used in section 4 in connection with Derjaguin-Landau-Verwey-Overbeek (DLVO) theory.

4. Discussion

Any decrease in permeability implies a decrease in the effective cross sectional area of the pore space that permits flow. In the present case this may occur by thermo-mechanical compaction of the rock yielding pore throat closure or unfavorable migration of clay particles within the pore space stimulated hydrodynamically, thermally, or chemically.

The key observations of this study that require discussion are as follows:

(1) Initially, all samples were saturated with deionized water but upon flow, permeability at room temperature remained high and only changed slightly (section 4.1).

(2) Increasing temperature stepwise to 145°C yielded a progressive and irreversible permeability decrease by 1.5 orders of magnitude in all samples regardless of the pore fluid composition investigated (section 4.2).

(3) Sample permeability decreased further when progressively diluting a previously introduced 2 M NaCl pore fluid below approximately 0.5 M. This observation was made both at room temperature and 145°C (section 4.3).

4.1. Hydraulic Sample Behavior at the Start

The application of DLVO theory for deionized water pore fluid conditions to our results suggests that repulsions between illite particles and between illite and the grain walls are strong (section 4.3). The fact that permeability remained high upon first saturation with deionized water implies that the clay fraction in this sandstone, initially, is strongly attached to the pore walls. Therefore, any permeability decrease observed later upon dilution of a saline NaCl pore fluid requires some kind of weakening mechanism by the subsequent fluid exchange that permits particle release upon flow.

Path-dependent permeability changes have been described before (Kwon et al., 2004; Mohan et al., 1993), indicating that high K^+ contents within the interlayer and the presence of divalent cations like Ca^{2+} or Mg^{2+} on the exchangeable sites of the crystal lattice have a stabilizing effect on the clay fraction in the pore space of sandstones (Mungan, 1968). The EMPA results presented in section 3.2 suggest that this is also the case for the illite clay in Flechtinger sandstone, at least initially and at room temperature. Consequently, when sample FS3 was initially flushed at room temperature with a substantial amount of deionized water (section 3.1) permeability only changed slightly. This observation was also made for sample FS4 although the respective fluid volume was smaller. This implies that an effect of purely hydrodynamic fines migration on permeability in the pristine rock is negligible at the applied flow rates. This conclusion is supported by the small mass loss measured for both samples FS1 and FS3 as well as the absence of fines migration evidenced by MIP for sample FS1 (section 3.2).

For samples FS3 and FS4 it was observed that an exchange of the preexisting deionized water pore fluid by a 2 M NaCl solution at room temperature resulted in a slight permeability increase (section 3.1). As was shown by Moore et al. (1982) for a swelling type of clay (montmorillonite), salinity-induced changes in electrical double layer (EDL) thickness result in variations of the size of clay particles that are exposed to the pore space and, consequently, of the effective cross sectional area available for flow of the free pore fluid. When increasing the salinity of the fluid, the thickness of the EDL decreases yielding an increase in permeability. Whether this mechanism, in fact, also operates in (nonswelling) illite needs to be investigated further but might yield hints to explain the present observations.

However, for longer time periods and enhanced by elevated temperatures, when deionized water in the pore space is exchanged for the highly concentrated NaCl solution, the partial replacement of the divalent cations of illite grains by Na^+ may occur, allowing more hydrodynamic dispersion of illite particles (Mungan, 1968; Rahman et al., 1995). Increased Na^+ content in sample FS3, as measured by EMPA (section 3.2) suggests that this weakening mechanism is important. At this stage the rock continues to behave in agreement with DLVO theory as will be shown below in section 4.3.

4.2. Effects of Temperature Changes

All samples in this study, FS1, FS3, and FS4, experienced substantial permeability reductions as temperature was increased from room temperature to 145°C regardless of the pore fluid composition, that is, deionized water or 2 M NaCl solution. Furthermore, this permeability damage was not recovered when temperature was decreased. This irreversible decrease was also not changed by reversing the direction of fluid flow.

The thermal strain of a rock resulting from heating generally contains elastic and inelastic components which are related to its microstructure and mineral composition (Gräf et al., 2013; Pei et al., 2016; Wong & Brace, 1979). Hence, any thermally induced permeability decline should be partially reversible when decreasing temperature. Evidently, this is in disagreement with the present observations suggesting that the pore throats were closed, at least partially, by compressive stresses resulting from thermal expansion of the rock matrix under confinement (McKay & Brigham, 1984; Somerton, 1980; Somerton et al., 1981; Weinbrandt et al., 1975). The degree of thermal strain that was attained at 80°C (FS1) or ultimately at 145°C (FS3 and FS4) reflects purely inelastic and thus irreversible deformation. Mechanistically this relates to the comparatively low mechanical strength of fine grained illite (e.g., Cebell & Chilingarian, 1972; Tanaka et al., 1997; Vaidya et al., 1973), the high illite content within the rock (i.e., 10 wt%), the illite microstructure in the pore space, and the fact that illite completely covers the pore walls (Figure 2). Overall, this reduces the load-bearing capacity of the rock at the pore scale yielding some degree of inelastic compaction sufficient to reduce the effective cross sectional area of the pore throats that, in combination, define the hydraulic properties of this sandstone (section 3.2; Figure 5).

Mineral dissolution reactions may also result in permanent changes of permeability (e.g., Yasuhara et al., 2015), particularly at elevated temperatures, since the dissolution rates will increase when heating a fluid-rock system that is in chemical disequilibrium. In contrast, cooling would potentially lead to oversaturation of some species in the pore fluid and thus mineral precipitation, consequently affecting permeability as well. However, in this study, after temperature was increased to the next level and had stabilized after a few hours (section 2.3) permeability was immediately measured and always showed to be less or equal to its value at the former (lower) temperature (Figure 3). This implies that the change (if any) likely had occurred concurrently to heating or shortly afterward. Moreover, a longer duration of stagnant flow (about 1 day) at elevated (maximum) temperature yielded no or only a marginal change in permeability (Appendix B) for both samples FS1 (deionized water; 141°C) and FS3 (2 M NaCl; 145°C). Not least, there is no indication of any substantial hydraulic effect of mineral precipitation upon cooling as permeability remained more or less constant as temperature was decreased to ambient conditions (Figure 3). Consequently, in this study, a significant effect of dissolution-precipitation reactions on the permeability of the sandstone samples during the temperature cycles is neither obvious nor likely as the respective rates of change differ significantly.

The SEM image of sample FS1 (Figure 4b) in comparison to sample S2 (Figure 4a) provides further evidence of compaction and irreversible pore throat closure after the experiment. This is supported by the MIP measurements in Figure 5a, where overall porosity of sample FS1 has decreased by partial disappearance of the

smallest pore throat-size fraction (i.e., 0.2 μm and below). Qualitatively sample FS3 has inherited the same microstructural changes during heating as sample FS1, but some features (Figures 4c and 5b) have evolved further as fluids were exchanged (section 4.3). The same should apply to sample FS4 that showed reproducible changes in absolute and relative permeability during heating.

In contrast to the similar reductions in permeability by magnitude, a minimum permeability threshold was only apparent for sample FS1 by 80°C (Figure 3a). For samples FS3 and FS4, up to 145°C, this was not obvious (Figures 3b and 3c). Whether this relates to the differences in pore fluid composition or subtle variations in sample microstructure is yet unclear and will require further investigations.

Our microstructural evidence demonstrates that permeability reductions with temperature measured in this study are thermo-mechanically induced. However, in other cases and particularly in kaolinite-bearing sandstones, elevated temperatures may favor clay detachment and migration as a result of amplified repulsive forces (e.g., García-García et al., 2006; Schembre et al., 2006; Schembre & Kovscek, 2005; You et al., 2015, 2016). The results of the MIP measurements for sample FS1 (Figure 5a) and negligible mass loss for both samples FS1 and FS3 (section 3.2) demonstrate that migration of fine particles is very limited in our heated samples, before fluids are exchanged. This is different from the behavior of sandstones dominated by kaolinite as the clay fraction (e.g., Rosenbrand et al., 2015; Schembre & Kovscek, 2005). Fine particle migration, in the present sandstones, becomes important when pore fluids are diluted from 2 M to below 0.5 M NaCl at room temperature and 145°C (section 4.3).

4.3. Effects of NaCl Salinity Changes

Permeability damage in clay-bearing sandstone following a decrease in pore fluid salinity has been observed and investigated in numerous prior studies (e.g., Gabriel & Inamdar, 1983; Khilar & Fogler, 1984; McDowell-Boyer et al., 1986; Mohan et al., 1993; Mohan & Fogler, 1997). DLVO theory has often been applied to explain these observations (e.g., Schembre & Kovscek, 2005; Sharma et al., 1985). In the following, this will be performed for a model sandstone of high quartz content with secondary illite that closely resembles Flechtinger sandstone. A sphere-plate model is used to express both illite particle-to-tangential illite interactions and illite particle-to-quartz grain surface interactions (Kia et al., 1987) (section 2.5; Figure 2). The general theory is summarized in Appendix A, and the parameterization specific to illite is outlined in the following.

The net surface charge of illite is approximately 1.60 mmol/g, while its cation exchange capacity (*CEC*) is typically in the range 0.10–0.40 mmol/g (Smith, 1967), resulting from some amount of nonexchangeable K^+ ions in the interlayer. The net surface charge density of illite σ_{illite} is related to the ratio between the *CEC* and the illite specific surface area S_a:

$$\sigma_{illite} = \frac{N_A \cdot e \cdot CEC}{S_a} \tag{5}$$

where N_A is the Avogadro constant and e is the elementary charge. The *CEC* depends on the net charge of the clay faces and is variable with pH. The charge of clay edges is generally negative in alkaline solutions and positive in acidic ones, while the charge of the crystal surfaces is negative in both cases (Al-Ani & Sarapää, 2008). Here, a pH-neutral environment is considered and the specific surface area of illite S_a is taken as 156 m^2/g (Kahr & Madsen, 1995). Based on the EMPA analysis (section 3.2) the *CEC* of illite is chosen to be either 0.11 or 0.05 mmol/g as maximum and median values, respectively, associated with the Na^+ content in illite of sample FS3. Finally, a salinity- and temperature-independent net surface charge density of illite is assumed, and all other temperature-dependent parameters are taken from literature as outlined in Appendix A.

The calculated total interaction free energy (Figure 7) may be attractive (negative) or repulsive (positive) at a given separation distance, depending on fluid salinity and temperature. For a NaCl salinity reduction from 2.0 to 0.5 M, illite-to-illite interactions continue to be attractive at either *CEC* (Figures 7a and 7b), and illite-quartz interactions are attractive at low *CEC* (0.05 mmol/g; Figure 7d). Repulsive forces and increases in the separation distance between the illite particles and the quartz surfaces are predicted by DLVO theory

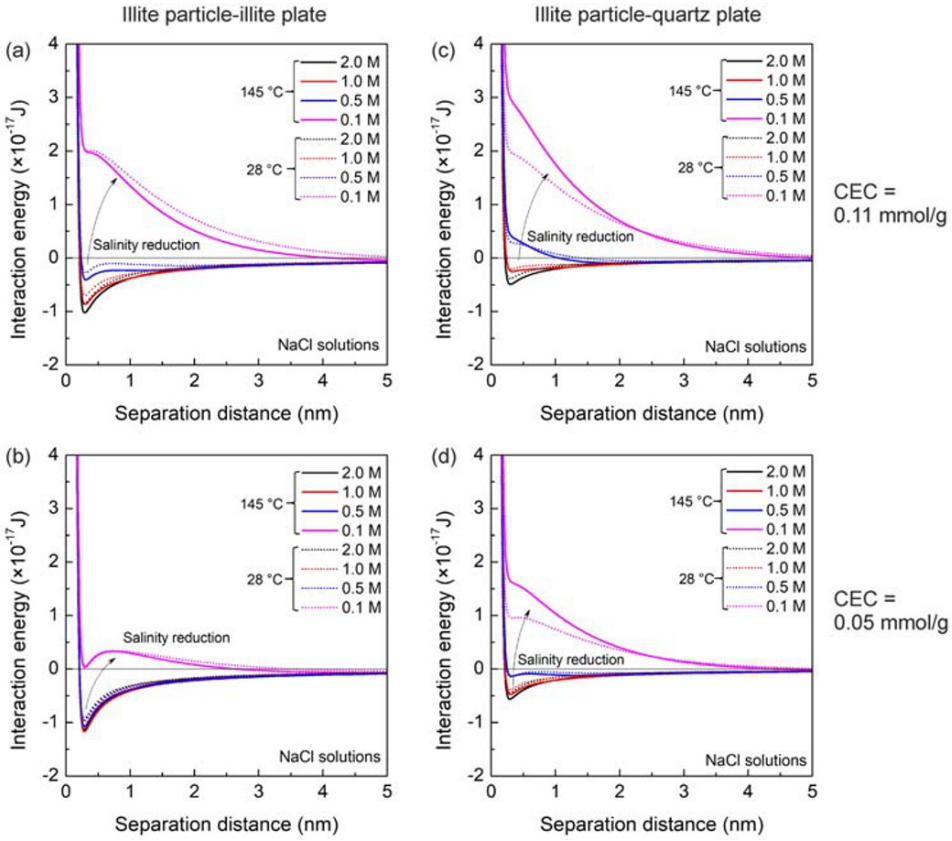

Figure 7. Total interaction free energy between illite particle and illite plate (a and b) and between illite particle and quartz plate (c and d) as a function of separation distance at 28°C (dashed lines), 145°C (solid lines), and at different NaCl salinities. A 0.1 M NaCl solution was used to illustrate the pore fluid exchange from 0.5 M NaCl to deionized water during the experiments with samples FS3 and FS4. The cation exchange capacity (*CEC*) is assumed to be 0.11 mmol/g in (a and c) and 0.05 mmol/g in (b and d), respectively.

only for high *CEC* (0.11 mmol/g, Figure 7c). Furthermore, temperature variations at temperatures between 28 and 145°C have a very minor effect on the respective energy-separation dependence at high salinity conditions (i.e., 0.5 to 2.0 M), particularly, when a low *CEC* (0.05 mmol/g; Figures 7b and 7d) is assumed.

Below NaCl concentrations of approximately 0.5 M the energy-separation dependences in Figure 7 become repulsive for all types of interactions and both *CEC*. To exemplify the trend for deionized water conditions, calculations were performed for an NaCl concentration of 0.1 M as shown in Figures 7a–7d. In this case, a temperature dependence of the respective interaction energy can be observed, particularly for illite-to-quartz interactions, and repulsion is realized at higher temperatures (Figures 7c and 7d).

In both experiments with samples FS3 (Figure 3b) and FS4 (Figure 3c) a further decrease in permeability was observed when a 0.5 M NaCl solution in the pore space was exchanged to deionized water, irrespective of the temperature (i.e., 28 or 145°C) at which this exchange was conducted. The SEM (Figure 4c) and MIP (Figure 5b) observations outlined in section 3.2 supported by the outcome of the DLVO calculations (Figure 7) above demonstrate that this decrease was due to clay particle mobilization and subsequent clogging of pores and pore throats with overall very minor mass loss toward the outside of the samples.

Virtually all pore walls are covered with illite (Figure 2); thus, it can be assumed that the pore fluid is mostly in contact with illite rather than quartz (or some other mineral constituent of the rock; Table 1). Mobilized particles thus would be predominantly pore lining and pore filling illite types (section 2.5; Figure 2). From Figures 7a and 7b (0.1 M NaCl lines) it can be inferred that the amount of released clay particles and the

release rate at a given fluid flow rate should only marginally depend on temperature. Moreover, a higher *CEC* favors and amplifies clay mobilization.

Once mobilized, illite particles may form a suspension with the pore fluid and migrate downstream as fluid flows through the rock until they are deposited in some pore constriction (Figure 4c). This behavior, now, is similar to that of kaolinite-bearing sandstones (e.g., Rosenbrand et al., 2015). From the upstream toward the downstream side of sample FS3 there is a progressive increase in the accumulation of particles reducing the effective sample porosity systematically and shifting the interval of the affected pore size fraction toward larger pore radii (Figure 5b).

5. Conclusions

Comprehensive flow-through experiments on permeability changes in illite-bearing (Rotliegend) sandstone were performed at multiple and systematically varied temperature and NaCl fluid salinity conditions. The experiments were complemented with an application of Derjaguin-Landau-Verwey-Overbeek (DLVO) theory and comparative microstructural investigations performed by scanning electron microscopy (SEM), electron microprobe analysis (EMPA), and mercury intrusion porosimetry (MIP) on both the starting material and the tested samples. The experimental and analytical observations were mechanistically interpreted yielding the following conclusions.

Permeability of sandstones containing illite as the dominant clay phase, even at substantial amounts, may be insensitive to changes in pore fluid salinity. This departure from DLVO theory predictions may be due to high K^+ and Ca^{2+} or Mg^{2+} contents within the illite crystal lattices. As a result, illite particles are strongly attached to the pore walls and resist hydrodynamic mobilization.

Permeability of illite-bearing sandstones with narrow pore throats dominating the rock's hydraulic properties may be very sensitive to heating, yielding (nearly) irreversible and thermo-mechanically induced pore throat closure. This effect is observed both for low (deionized water) and high (2 M NaCl solution) pore fluid salinity.

When an initially present low salinity fluid (i.e., deionized water in the case) is exchanged by a high salinity NaCl solution (e.g., 2 M) before heating, a partial replacement of the divalent ions in the illite crystal lattices by Na^+ may occur, as detected by EMPA. This yields an additional reduction in permeability as NaCl pore fluid salinity is subsequently decreased to below 0.5 M. This permeability reduction is observed at high temperature (i.e., 145°C) and at room temperature and is in agreement with predictions from DLVO theory. Mechanistically, this permeability decrease is chemically induced and results from clay particle mobilization, transport, and subsequent deposition in pores and pore throats.

In summary, illite-bearing sandstones may show substantial and largely irreversible permeability variations following temperature and fluid salinity changes. The respective underlying thermo-mechanical and chemical processes identified operate independently but are path dependent with respect to the applied fluid salinity sequence. Any such natural or geotechnically used rock system may thus be susceptible to permeability reduction with consequences for the evolution of fluid flow when changes in the here investigated parameters occur or are induced.

Appendix A: Calculation of the Particle Interaction Energy by DLVO Theory

According to DLVO theory, the total interaction free energy between two (solid) phases in an aqueous solution can be calculated by combining the London-van der Waals attraction V_{vdW} and the, commonly repulsive, electrical double layer (EDL) interaction V_{EDL} (Leite et al., 2012). In addition, the extended Born potential V_{BR} is a short-range (<0.5 nm) molecular interaction resulting from the overlap of electron clouds. Its magnitude is negligible in comparison to V_{vdW} and V_{EDL} for particle separations larger than 0.5 nm (Khilar & Fogler, 1987). In the following, all other possible interactions (e.g., Tchistiakov, 2000) are neglected and the total interaction free energy thus is expressed as

$$V_{total} = V_{EDL} + V_{vdW} + V_{BR} \tag{A1}$$

Considering a sphere-plate geometry, the van der Waals interaction free energy at a separation distance d is defined as (Bergström, 1997; Gregory, 1981)

$$V_{vdW}^{i,i}(d) = -\frac{A_{131} r_p}{6d} \tag{A2a}$$

for illite particle to illite plate interactions and

$$V_{vdW}^{q,i}(d) = -\frac{A_{132} r_p}{6d} \tag{A2b}$$

for illite particle to quartz plate interactions, respectively, where r_p is the particle radius. Here and based on the SEM observations (Figure 2), an average particle radius of 1.2 μm is assumed. The Hamaker constant A characterizes the interaction between clay minerals (subscript 1) and the grain walls (subscript 2) separated by an aqueous fluids (subscript 3) (Israelachvili, 2011)

$$A_{131} = \frac{3k_B T}{4}\left(\frac{\varepsilon_1 - \varepsilon_3}{\varepsilon_1 + \varepsilon_3}\right)^2 + \frac{3h\nu_e}{16\sqrt{2}}\frac{\left(n_1^2 - n_3^2\right)^2}{\left(n_1^2 + n_3^2\right)^{\frac{3}{2}}} \tag{A3a}$$

$$A_{132} = \frac{3k_B T}{4}\left(\frac{\varepsilon_1 - \varepsilon_3}{\varepsilon_1 + \varepsilon_3}\right)\left(\frac{\varepsilon_2 - \varepsilon_3}{\varepsilon_2 + \varepsilon_3}\right) + \frac{3h\nu_e}{8\sqrt{2}}\frac{\left(n_1^2 - n_3^2\right)\left(n_2^2 - n_3^2\right)}{\left(n_1^2 + n_3^2\right)^{\frac{1}{2}}\left(n_2^2 + n_3^2\right)^{\frac{1}{2}}\left[\left(n_1^2 + n_3^2\right)^{\frac{1}{2}} + \left(n_2^2 + n_3^2\right)^{\frac{1}{2}}\right]} \tag{A3b}$$

where $k_B = 1.381 \times 10^{-23}$ J/K is the Boltzmann constant, T is the absolute temperature, and $h = 6.626 \times 10^{-34}$ Js is the Planck constant. ε_1, ε_2, and ε_3 are the dielectric permittivities, n_1, n_2, and n_3 are the refractive indexes, and the subscripts 1, 2, and 3 denote clay, quartz, and NaCl solution, respectively. $\nu_e = 3 \times 10^{15}$ s^{-1} is the main electronic absorption frequency (Israelachvili, 2011). The dielectric permittivity of illite ε_1 is taken from Josh and Clennell (2015). The dielectric permittivity of quartz ε_2 is independent of temperature in the range between 20 and 175°C according to Stuart (1955). Finally, the temperature and salinity dependent dielectric permittivity of an NaCl solution ε_3 is given, for example, by Marshall (2008) and Maribo-Mogensen et al. (2013). A constant refractive index $n_1 = 1.59$ is assumed (Friedrich et al., 2008), and the temperature-dependent indices n_2 and n_3 are taken from Leviton and Frey (2006) and Aly and Esmail (1993), respectively.

According to Gouy-Chapman theory (Butt et al., 2006), the net surface charge density σ_{illite} defines the surface potential Ψ_1 of illite as expressed by the Grahame (1947) equation:

$$\Psi_1 = \frac{2k_B T}{ze}\ln\left(\frac{\sigma_{illite}}{\sqrt{8N_A c\varepsilon_0\varepsilon_r k_B T}} + \sqrt{\frac{\sigma_{illite}^2}{8N_A c\varepsilon_0\varepsilon_r k_B T} + 1}\right) \tag{A4}$$

where c is the cation concentration in the solution, z is the valence of the respective cation, e is the elementary charge, and N_A is the Avogadro constant. $\varepsilon_0 = 8.854 \times 10^{12}$ C^2/Nm^2 is the vacuum permittivity, and ε_r is the relative permittivity of the solvent given by Maribo-Mogensen et al. (2013). The counter-ions that extend from a negatively charged surface into the aqueous solution result in a diffuse EDL. The thickness of this EDL is known as the Debye screening length κ^{-1}, which is expressed as

$$\kappa^{-1} = \sqrt{\frac{\varepsilon_0\varepsilon_r k_B T}{N_A c e^2 z^2}} \tag{A5}$$

Assuming a constant surface charge density where the surface charges are uniformly distributed on the illite crystals, the surface potentials of two illite phases are equal. Consequently, the interaction free energy of the EDL for the illite particle to illite plate system is (Gregory, 1975):

$$V_{EDL}^{i,i}(d) = 64\pi r_p k_B T N_A c z^2 \kappa^{-2}\tanh^2\left(\frac{ze\Psi_1}{4k_B T}\right)e^{-\kappa d} \tag{A6a}$$

Similarly, for the illite particle to quartz plate system the interaction free energy is

$$V_{EDL}^{q,i}(d) = 64\pi r_p k_B T N_A c z^2 \kappa^{-2} \tanh\left(\frac{ze\Psi_1}{4k_B T}\right) \tanh\left(\frac{ze\Psi_2}{4k_B T}\right) e^{-\kappa d} \quad \text{(A6b)}$$

where the surface potential of quartz Ψ_2, approximated by the zeta potential, is temperature dependent (Ramachandran & Somasundaran, 1986; Rodríguez & Araujo, 2006; Schembre & Kovscek, 2005) and decreases as temperature increases.

Finally, the extended Born potential is expressed as (Ruckenstein & Prieve, 1976):

$$V_{BR}(d) = \frac{A\sigma_c^6}{7560}\left[\frac{8r_p + d}{(2r_p + d)^7} + \frac{6r_p - d}{d^7}\right] \quad \text{(A7)}$$

where the collision diameter $\sigma_c = 0.5$ nm is assumed to be constant (Elimelech et al., 2013).

Appendix B: Experimental Data of the Permeability Measurements

Table B1
Sample FS1

No.	Stage	Temperature (°C)	Permeability (mD)	Max flow rate (ml/min)	Fluid	Total time (hr)	Flow direction
1	1	25	5.016	2	H_2O	2	Bottom to top
2		40	3.407	2	H_2O	8	—
3		58	0.636	1	H_2O	27	—
4		76	0.254	0.3	H_2O	35	—
5		79	0.184	0.25	H_2O	98	—
6		96	0.155	0.2	H_2O	103	—
7		117	0.143	0.2	H_2O	108	—
8		119	0.158	0.2	H_2O	123	—
9		140	0.197	0.4	H_2O	127	—
10	2	121	0.209	0.3	H_2O	132	—
11		118	0.217	0.3	H_2O	146	—
12		97	0.205	0.3	H_2O	152	—
13		81	0.193	0.25	H_2O	155	—
14		80	0.191	0.25	H_2O	156	—
15		61	0.175	0.1	H_2O	173	—
16		43	0.158	0.05	H_2O	197	—
17	3	60	0.168	0.1	H_2O	202	—
18		78	0.168	0.2	H_2O	222	—
19		95	0.182	0.2	H_2O	248	—
20		118	0.212	0.3	H_2O	270	—
21		141	0.212	0.4	H_2O	274	—
22	4	141	0.222	0.5	H_2O	296	—
23		120	0.229	0.4	H_2O	321	—
24		96	0.223	0.3	H_2O	342	—
25		80	0.222	0.3	H_2O	367	—
26		61	0.190	0.15	H_2O	391	—
27		43	0.183	0.1	H_2O	412	—
28		43	0.151	0.05	H_2O	606	—
29	5	43	0.144	0.05	H_2O	804	Top to bottom
30		43	0.145	0.05	H_2O	846	—
31		43	0.144	0.05	H_2O	1,281	—

Notes. Stages 1–4 indicate the respective temperature increase or decrease; during Stage 5 the flow direction was reversed.

Table B2
Sample FS3

No.	Stage	Temperature (°C)	Permeability (mD)	Max flow rate (ml/min)	Fluid	Total volume (ml)	Flow time (hr)	Cumulative flow time (hr)	Total time (hr)	Flow direction
1	1	25	25.229	2	H_2O	176	3.17	3.17	4	Bottom to top
2		25	22.777	2	H_2O	380	3	6.17	22	—
3		25	21.258	1	H_2O	594	3.63	9.8	50	—
4		25	17.007	1	H_2O	794	3.33	13.13	74	—
5		25	16.673	1	H_2O	836	0.68	13.81	284	—
6		25	16.673	1	H_2O	1,082	4.1	17.91	290	—
7	2	25	16.673	1	H_2O	1,101	0.32	18.23	525	—
8		25	19.013	1	2.0 M Na	1,116	0.25	18.48	552	—
9		41	12.148	1	2.0 M Na	1,126.5	0.17	18.65	622	—
10		61	7.493	1	2.0 M Na	1,133.5	0.12	18.77	625	—
11		81	3.970	1	2.0 M Na	1,139.5	0.1	18.87	642	—
12		98	2.216	1	2.0 M Na	1,144.5	0.08	18.95	645	—
13		121	1.150	1	2.0 M Na	1,148.5	0.07	19.02	649	—
14		145	0.606	1	2.0 M Na	1154.5	0.1	19.12	666	—
15	3	145	0.621	1	2.0 M Na	1,158.5	0.07	19.19	693	—
16		145	0.598	1	1.0 M Na	1,170.5	0.2	19.39	713	—
17		145	0.524	1	0.5 M Na	1,193.5	0.38	19.77	715	—
18		145	0.020	0.03	H_2O	1,195.74	1.3	21.07	720	—
19	4	121	0.024	0.03	H_2O	1,200.42	2.67	23.74	747	—
20		99	0.025	0.03	H_2O	1,207.225	3.8	27.54	789	—
21		81	0.026	0.03	H_2O	1,212.98	3.2	30.74	813	—
22		61	0.029	0.03	H_2O	1,218.418	3	33.74	836	—
23		41	0.036	0.03	H_2O	1,223.446	2.8	36.54	860	—
24		29	0.035	0.02	H_2O	1,252.074	23.8	60.34	1,049	—

Notes. Stage 1: flow-through experiment with a large volume of deionized water; Stage 2: fluid exchange and temperature increase from 25 to 145°C; Stage 3: salinity decrease from 2 M NaCl to deionized water at 145°C; Stage 4: temperature decrease from 145°C to room temperature.

Table B3
Sample FS4

No.	Stage	Temperature (°C)	Permeability (mD)	Max flow rate (ml/min)	Fluid	Total volume (ml)	Flow time (hr)	Cumulative flow time (hr)	Total time (hr)	Flow direction
1	1	27	24.295	2	H_2O	14.45	0.2	0.2	1	Bottom to top
2		27	24.295	2	H_2O	19.45	0.08	0.28	69	—
3		27	22.982	1	H_2O	24.45	0.08	0.37	117	—
4		27	22.982	1	H_2O	26.95	0.05	0.42	141	—
5	2	27	21.803	1	H_2O	31.95	0.08	0.5	262	—
6		27	22.817	1	2.0 M Na	44.95	0.27	0.77	263	—
7		42	19.177	1	2.0 M Na	49.95	0.08	0.85	268.5	—
8		62	10.218	1	2.0 M Na	57.45	0.13	0.97	284.5	—
9		81	4.502	1	2.0 M Na	60.95	0.06	1.03	292.5	—
10		100	2.532	1	2.0 M Na	63.95	0.05	1.08	308.5	—
11		122	0.651	1	2.0 M Na	66.95	0.05	1.13	332.5	—
12		145	0.445	0.5	2.0 M Na	69.95	0.1	1.23	340	—
13	3	122	0.468	0.5	2.0 M Na	72.35	0.08	1.32	405	—
14		100	0.475	0.5	2.0 M Na	75.35	0.1	1.42	412	—
15		81	0.502	0.5	2.0 M Na	78.75	0.1	1.52	429	—
16		62	0.526	0.4	2.0 M Na	82.55	0.16	1.67	436.5	—
17		42	0.561	0.3	2.0 M Na	84.45	0.1	1.77	452.5	—
18		29	0.565	0.2	2.0 M Na	86.45	0.17	1.94	475.3	—
19	4	28	0.542	0.2	1.0 M Na	93.75	0.61	2.55	477.3	—
20		28	0.519	0.2	0.5 M Na	103.5	0.81	3.36	479	—
21		28	0.009	0.002	H_2O	114.13	22	25.36	502	—
22		28	0.010	0.003	H_2O	119.204	26	51.36	528	—
23		27	0.009	0.005	H_2O	137.219	44	95.36	957	—

Note. Stage 1: flow-through experiment with a small volume of deionized water; Stage 2: fluid exchange and temperature increase from 25 to 145°C; Stage 3: temperature decrease from 145°C to room temperature; Stage 4: salinity decrease from 2 M NaCl to deionized water at room temperature. FS4 underwent additional procedures beyond Stage 4 which are excluded from the present study.

Data Availability Statement

In addition to being fully documented within this paper, all experimental data were submitted to the GFZ Data Repository for public availability and can be accessed online (10.5880/GFZ.4.8.2020.005).

Acknowledgments

The authors wish to express their gratitude to Dr. Anja Schleicher (X-Ray Diffraction Lab, GFZ) for XRD measurements and analysis, Dr. Franziska Wilke (Microprobe Lab, GFZ) for the EMPA analysis, Christian Cunow for the help with mercury intrusion porosimetry measurements, and Ilona Schäpan (SEM Lab, GFZ) for SEM measurements. Chaojie Cheng is grateful for constructive discussions with Prof. Michael Kühn (GFZ and University of Potsdam) and Prof. Christoph Hilgers (Karlsruhe Institute of Technology, KIT). Chaojie Cheng was funded by the China Scholarship Council (grant no. 201606410056), and this work was supported by the German Federal Ministry of Economic Affairs and Energy (BMWi) under grant no. 0324065. We also thank the editor, Yves Bernabé, and two reviewers, Diane Moore and Andreas Kronenberg, for constructive and valuable comments on the manuscript that helped to improve this paper. Open access funding enabled and organized by Projekt DEAL.

References

Al-Ani, T., & Sarapää, O. (2008). *Clay and clay mineralogy: Physical-chemical properties and industrial uses*. Finland: Geological Survey of Finland.

Aly, K. M., & Esmail, E. (1993). Refractive index of salt water: Effect of temperature. *Optical Materials*, *2*(3), 195–199. https://doi.org/10.1016/0925-3467(93)90013-Q

Anderson, R. L., Ratcliffe, I., Greenwell, H. C., Williams, P. A., Cliffe, S., & Coveney, P. V. (2010). Clay swelling—A challenge in the oilfield. *Earth-Science Reviews*, *98*(3–4), 201–216. https://doi.org/10.1016/j.earscirev.2009.11.003

Azari, M., & Leimkuhler, J. M. (1990). Formation permeability damage induced by completion brines. *Journal of Petroleum Technology*, *42*(04), 486–492. https://doi.org/10.2118/17149-PA

Baudracco, J., & Aoubouazza, M. (1995). Permeability variations in Berea and Vosges sandstone submitted to cyclic temperature percolation of saline fluids. *Geothermics*, *24*(5–6), 661–677. https://doi.org/10.1016/0375-6505(95)00027-5

Bedrikovetsky, P., Siqueira, F. D., Furtado, C. A., & Souza, A. L. S. (2011). Modified particle detachment model for colloidal transport in porous media. *Transport in Porous Media*, *86*(2), 353–383. https://doi.org/10.1007/s11242-010-9626-4

Bedrikovetsky, P., Zeinijahromi, A., Siqueira, F. D., Furtado, C. A., & de Souza, A. L. S. (2012). Particle detachment under velocity alternation during suspension transport in porous media. *Transport in Porous Media*, *91*(1), 173–197. https://doi.org/10.1007/s11242-011-9839-1

Bergström, L. (1997). Hamaker constants of inorganic materials. *Advances in Colloid and Interface Science*, *70*, 125–169. https://doi.org/10.1016/S0001-8686(97)00003-1

Bhattacharjee, S., Elimelech, M., & Borkovec, M. (1998). DLVO interaction between colloidal particles: Beyond Derjaguin's approximation. *Croatica Chemica Acta*, *71*(4), 883–903. Retrieved from https://hrcak.srce.hr/132427

Brown, G. O. (2002). Henry Darcy and the making of a law. *Water Resources Research*, *38*(7), 111–112. https://doi.org/10.1029/2001WR000727

Butt, H. J., Graf, K., & Kappl, M. (2006). *Physics and chemistry of interfaces*. Weinheim: John Wiley & Sons.

Casse, F. J., & Ramey, H. J. (1979). The effect of temperature and confining pressure on single-phase flow in consolidated rocks. *Journal of Petroleum Technology*, *31*(08), 1051–1059. https://doi.org/10.2118/5877-PA

Cebell, W. A., & Chilingarian, G. V. (1972). Some data on compressibility and density anomalies in halloysite, hectorite, and illite clays. *AAPG Bulletin*, *56*(4), 796–802. https://doi.org/10.1306/819A4086-16C5-11D7-8645000102C1865D

Cheng, C., & Milsch, H. (2020). *Experimental rock permeability data for illite-bearing Flechtinger sandstone measured with a flow-through apparatus at GFZ Potsdam*. Potsdam, Germany: GFZ Data Services. https://doi.org/10.5880/GFZ.4.8.2020.005

Cooper, J. R. (2008). *Release on the IAPWS formulation 2008 for the viscosity of ordinary water substance* (pp. R12–R08). Berlin, Germany: IAPWS.

Darcy, H. (1856). *Les fontaines publique de la ville de Dijon*. Paris, France: Dalmont.

Deraguin, B., & Landau, L. (1941). Theory of the stability of strongly charged lyophobic sols and of the adhesion of strongly charged particles in solution of electrolytes. *Acta Physicochim: USSR*, *14*, 633–662. https://doi.org/10.1016/0079-6816(93)90013-L

Desbois, G., Urai, J. L., Hemes, S., Schröppel, B., Schwarz, J.-O., Mac, M., & Weiel, D. (2016). Multi-scale analysis of porosity in diagenetically altered reservoir sandstone from the Permian Rotliegend (Germany). *Journal of Petroleum Science and Engineering*, *140*, 128–148. https://doi.org/10.1016/j.petrol.2016.01.019

Elimelech, M., Gregory, J., & Jia, X. (2013). *Particle deposition and aggregation: Measurement, modelling and simulation*. Oxford, England: Butterworth-Heinemann.

Friedrich, F., Steudel, A., & Weidler, P. G. (2008). Change of the refractive index of illite particles by reduction of the Fe content of the octahedral sheet. *Clays and Clay Minerals*, *56*(5), 505–510. https://doi.org/10.1346/CCMN.2008.0560503

Gabriel, G., & Inamdar, G. (1983). *An experimental investigation of fines migration in porous media*. Paper presented at SPE Annual Technical Conference and Exhibition, San Francisco, CA, USA, Society of Petroleum Engineers, Richardson, TX. https://doi.org/10.2118/12168-MS

García-García, S., Jonsson, M., & Wold, S. (2006). Temperature effect on the stability of bentonite colloids in water. *Journal of Colloid and Interface Science*, *298*(2), 694–705. https://doi.org/10.1016/j.jcis.2006.01.018

Gobran, B. D., Brigham, W. E., & Ramey, H. J. Jr. (1987). Absolute permeability as a function of confining pressure, pore pressure, and temperature. *SPE Formation Evaluation*, *2*(01), 77–84. https://doi.org/10.2118/10156-PA

Gräf, V., Jamek, M., Rohatsch, A., & Tschegg, E. (2013). Effects of thermal-heating cycle treatment on thermal expansion behavior of different building stones. *International Journal of Rock Mechanics and Mining Sciences*, *64*, 228–235. https://doi.org/10.1016/j.ijrmms.2013.08.007

Grahame, D. C. (1947). The electrical double layer and the theory of electrocapillarity. *Chemical Reviews*, *41*(3), 441–501. https://doi.org/10.1021/cr60130a002

Gray, D. H. (1966). Formation damage in sandstones caused by clay dispersion and migration. *Clays and Clay Minerals*, *14*(1), 355–366. https://doi.org/10.1346/ccmn.1966.0140131

Gregory, J. (1975). Interaction of unequal double layers at constant charge. *Journal of Colloid and Interface Science*, *51*(1), 44–51. https://doi.org/10.1016/0021-9797(75)90081-8

Gregory, J. (1981). Approximate expressions for retarded van der Waals interaction. *Journal of Colloid and Interface Science*, *83*(1), 138–145. https://doi.org/10.1016/0021-9797(81)90018-7

Guildner, L. A., Johnson, D. P., & Jones, F. E. (1976). Vapor pressure of water at its triple point. *Journal of Research of the National Bureau of Standards - A Physics and Chemistry*, *80A*(3), 505–521. https://doi.org/10.6028/jres.080A.054

Huenges, E. (2010). *Geothermal energy systems: Exploration, development, and utilization*. Weinheim: Wiley-VCH.

Israelachvili, J. N. (2011). *Intermolecular and surface forces*. Amsterdam, The Netherlands: Elsevier.

Jing, X. D. (1990). *The effect of clay, pressure and temperature on the electrical and hydraulic properties of real and synthetic rocks* (Doctoral dissertation). London, UK: Imperial College London (University of London).

Joseph, K., Khalifa, H. E., & Correia, R. J. (1981). Tables of the dynamic and kinematic viscosity of aqueous NaCl solutions in the temprature range 20-150°C and the pressure range 0.1–35 MPa. *American Institute of Physics and the American Chemical Society*, *10*(1), 71–88. https://doi.org/10.1063/1.555641

Josh, M., & Clennell, B. (2015). Broadband electrical properties of clays and shales: Comparative investigations of remolded and preserved samples. *Geophysics*, *80*(2), D129–D143. https://doi.org/10.1190/geo2013-0458.1

Juanes, R., Spiteri, E. J., Orr, F. M., & Blunt, M. J. (2006). Impact of relative permeability hysteresis on geological CO_2 storage. *Water Resources Research*, *42*, W12418. https://doi.org/10.1029/2005WR004806

Kahr, G., & Madsen, F. T. (1995). Determination of the cation exchange capacity and the surface area of bentonite, illite and kaolinite by methylene blue adsorption. *Applied Clay Science*, *9*(5), 327–336. https://doi.org/10.1016/0169-1317(94)00028-O

Khilar, K. C., & Fogler, H. S. (1983). Water sensitivity of sandstones. *Society of Petroleum Engineers Journal*, *23*(01), 55–64. https://doi.org/10.2118/10103-PA

Khilar, K. C., & Fogler, H. S. (1984). The existence of a critical salt concentration for particle release. *Journal of Colloid and Interface Science*, *101*(1), 214–224. https://doi.org/10.1016/0021-9797(84)90021-3

Khilar, K. C., & Fogler, H. S. (1987). Colloidally induced fines migration in porous media. *Reviews in Chemical Engineering*, *4*(1–2), 41–108. https://doi.org/10.1515/REVCE.1987.4.1-2.41

Kia, S., Fogler, H. S., & Reed, M. (1987). *Effect of salt composition on clay release in Berea sandstones*. Paper presented at SPE International Symposium on Oilfield Chemistry, San Antonio, Texas, USA, Society of Petroleum Engineers, Richardson, TX. https://doi.org/10.2118/16254-MS

Kwon, O., Herbert, B. E., & Kronenberg, A. K. (2004). Permeability of illite-bearing shale: 2. Influence of fluid chemistry on flow and functionally connected pores. *Journal of Geophysical Research*, *109*, B10206. https://doi.org/10.1029/2004JB003055

Leite, F. L., Bueno, C. C., Da Roz, A. L., Ziemath, E. C., & Oliveira, O. N. (2012). Theoretical models for surface forces and adhesion and their measurement using atomic force microscopy. *International Journal of Molecular Sciences*, *13*(12), 12,773–12,856. https://doi.org/10.3390/ijms131012773

Leviton, D. B., & Frey, B. J. (2006). *Temperature-dependent absolute refractive index measurements of synthetic fused silica*. Paper presented at Optomechanical Technologies for Astronomy, Orlando, Florida, USA, SPIE, Bellingham, WA. https://doi.org/10.1117/12.672853

Maribo-Mogensen, B., Kontogeorgis, G. M., & Thomsen, K. (2013). Modeling of dielectric properties of aqueous salt solutions with an equation of state. *The Journal of Physical Chemistry B*, *117*(36), 10,523–10,533. https://doi.org/10.1021/jp403375t

Marshall, W. L. (2008). Dielectric constant of water discovered to be simple function of density over extreme ranges from −35 to +600°C and to 1200 MPa (12000 Atm.), believed universal. *Nature Precedings*. https://doi.org/10.1038/npre.2008.2472.1

McDowell-Boyer, L. M., Hunt, J. R., & Sitar, N. (1986). Particle transport through porous media. *Water Resources Research*, *22*(13), 1901–1921. https://doi.org/10.1029/WR022i013p01901

McKay, W. I., & Brigham, W. E. (1984). *Effects of temperature on the absolute permeability of consolidated sandstone*. CA, USA: Petroleum Research Institute, Stanford University.

Milsch, H., Spangenberg, E., Kulenkampff, J., & Meyhöfer, S. (2008). A new apparatus for long-term petrophysical investigations on geothermal reservoir rocks at simulated in-situ conditions. *Transport in Porous Media*, *74*(1), 73–85. https://doi.org/10.1007/s11242-007-9186-4

Mohan, K. K., & Fogler, H. S. (1997). Effect of pH and layer charge on formation damage in porous media containing swelling clays. *Langmuir*, *13*(10), 2863–2872. https://doi.org/10.1021/la960868w

Mohan, K. K., Fogler, H. S., Vaidya, R. N., & Reed, M. G. (1993). Water sensitivity of sandstones containing swelling and non-swelling clays. *Colloids and Surfaces A: Physicochemical and Engineering Aspects*, *73*, 237–254. https://doi.org/10.1016/0927-7757(93)80019-B

Moore, D. E., Morrow, C. A., & Byerlee, J. D. (1982). Use of swelling clays to reduce permeability and its potential application to nuclear waste repository sealing. *Geophysical Research Letters*, *9*(9), 1009–1012. https://doi.org/10.1029/GL009i009p01009

Mungan, N. (1968). Permeability reduction due to salinity changes. *Journal of Canadian Petroleum Technology*, *7*(03), 113–117. https://doi.org/10.2118/68-03-04

Musharova, D., Mohamed, I. M., & Nasr-El-Din, H. A. (2012). *Detrimental effect of temperature on fines migration in sandstone formations*. Paper presented at SPE International Symposium and Exhibition on Formation Damage Control, Louisiana, USA, Society of Petroleum Engineers, Richardson, TX. https://doi.org/10.2118/150953-MS

Omar, A. E. (1990). Effect of brine composition and clay content on the permeability damage of sandstone cores. *Journal of Petroleum Science and Engineering*, *4*(3), 245–256. https://doi.org/10.1016/0920-4105(90)90014-T

Pei, L., Blöcher, G., Milsch, H., Deon, F., Zimmermann, G., Rühaak, W., et al. (2016). Thermal strain in a water-saturated limestone under hydrostatic and deviatoric stress states. *Tectonophysics*, *688*, 49–64. https://doi.org/10.1016/j.tecto.2016.09.020

Potter, J. M., Nur, A., & Dibble, W. E., Jr. (1980). *Effect of temperature and solution composition on the permeability of St. Peters sandstone: Role of iron (III)*. Stanford, CA: Department of Geology, Stanford University.

Rahman, S. S., Rahman, M. M., & Khan, F. A. (1995). Response of low-permeability, illitic sandstone to drilling and completion fluids. *Journal of Petroleum Science and Engineering*, *12*(4), 309–322. https://doi.org/10.1016/0920-4105(94)00052-6

Ramachandran, R., & Somasundaran, P. (1986). Effect of temperature on the interfacial properties of silicates. *Colloids and Surfaces*, *21*, 355–369. https://doi.org/10.1016/0166-6622(86)80104-4

Rodríguez, K., & Araujo, M. (2006). Temperature and pressure effects on zeta potential values of reservoir minerals. *Journal of Colloid and Interface Science*, *300*(2), 788–794. https://doi.org/10.1016/j.jcis.2006.04.030

Rosenbrand, E., Kjoller, C., Riis, J. F., Kets, F., & Fabricius, I. L. (2015). Different effects of temperature and salinity on permeability reduction by fines migration in Berea sandstone. *Geothermics*, *53*, 225–235. https://doi.org/10.1016/j.geothermics.2014.06.004

Ruckenstein, E., & Prieve, D. C. (1976). Adsorption and desorption of particles and their chromatographic separation. *AICHE Journal*, *22*(2), 276–283. https://doi.org/10.1002/aic.690220209

Russell, T., Wong, K., Zeinijahromi, A., & Bedrikovetsky, P. (2018). Effects of delayed particle detachment on injectivity decline due to fines migration. *Journal of Hydrology*, *564*, 1099–1109. https://doi.org/10.1016/j.jhydrol.2018.07.067

Schembre, J., & Kovscek, A. (2005). Mechanism of formation damage at elevated temperature. *Journal of Energy Resources Technology*, *127*(3), 171–180. https://doi.org/10.1115/1.1924398

Schembre, J., Tang, G.-Q., & Kovscek, A. (2006). Wettability alteration and oil recovery by water imbibition at elevated temperatures. *Journal of Petroleum Science and Engineering*, *52*(1–4), 131–148. https://doi.org/10.1016/j.petrol.2006.03.017

Sharma, M. M., Yortsos, Y. C., & Handy, L. L. (1985). *Release and deposition of clays in sandstones*. Paper presented at SPE Oilfield and Geothermal Chemistry Symposium, Phoenix, Arizona, USA, Society of Petroleum Engineers, Richardson, TX. https://doi.org/10.2118/13562-MS

Smith, S. J. (1967). *Susceptibility of interlayer potassium in illites to exchange* (Doctoral dissertation). Ames, IA: Iowa State University of Science and Technology.

Somerton, W. (1980). Some physical properties of Cerro Prieto cores. *Geothermics*, *9*(1–2), 159–168. https://doi.org/10.1016/0375-6505(80)90029-2

Somerton, W. H. (1992). *Thermal properties and temperature-related behavior of rock/fluid systems*. Amsterdam, The Netherlands: Elsevier.

Somerton, W. H., Janah, A. H., & Ashqar, P. I. (1981). *Thermal expansion of fluid saturated rocks under stress*. Paper presented at SPWLA 22nd Annual Logging Symposium, Mexico City, Mexico, Society of Petrophysicists and Well-Log Analysts, Houston, TX.

Stuart, M. R. (1955). Dielectric constant of quartz as a function of frequency and temperature. *Journal of Applied Physics*, *26*(12), 1399–1404. https://doi.org/10.1063/1.1721922

Sun, Y. Z., Xie, L. Z., He, B., Gao, C., & Wang, J. (2016). Effects of effective stress and temperature on permeability of sandstone from CO_2-plume geothermal reservoir. *Journal of Rock Mechanics and Geotechnical Engineering*, *8*(6), 819–827. https://doi.org/10.1016/j.jrmge.2016.07.004

Sundberg, J., Back, P.-E., Christiansson, R., Hökmark, H., Ländell, M., & Wrafter, J. (2009). Modelling of thermal rock mass properties at the potential sites of a Swedish nuclear waste repository. *International Journal of Rock Mechanics and Mining Sciences*, *46*(6), 1042–1054. https://doi.org/10.1016/j.ijrmms.2009.02.004

Tanaka, N., Graham, J., & Crilly, T. (1997). Stress-strain behaviour of reconstituted illitic clay at different temperatures. *Engineering Geology*, *47*(4), 339–350. https://doi.org/10.1016/S0013-7952(96)00113-5

Tchistiakov, A. A. (2000). *Colloid chemistry of in-situ clay-induced formation damage*. Paper presented at SPE International Symposium on Formation Damage Control, Lafayette, Louisiana, USA, Society of Petroleum Engineers, Richardson, TX. https://doi.org/10.2118/58747-MS

Vaidya, S., Bailey, S., Pasternack, T., & Kennedy, G. (1973). Compressibility of fifteen minerals to 45 kilobars. *Journal of Geophysical Research*, *78*(29), 6893–6898. https://doi.org/10.1029/JB078i029p06893

Verwey, E. J. W. (1947). Theory of the stability of lyophobic colloids. *The Journal of Physical Chemistry*, *51*(3), 631–636. https://doi.org/10.1021/j150453a001

Washburn, E. W. (1921). The dynamics of capillary flow. *Physical Review*, *17*(3), 273–283. https://doi.org/10.1103/PhysRev.17.273

Wei, K. K., Morrow, N. R., & Brower, K. R. (1986). Effect of fluid, confining pressure, and temperature on absolute permeabilities of low-permeability sandstones. *SPE Formation Evaluation*, *1*(04), 413–423. https://doi.org/10.2118/13093-PA

Weinbrandt, R., Ramey, H. Jr., & Casse, F. (1975). The effect of temperature on relative and absolute permeability of sandstones. *Society of Petroleum Engineers Journal*, *15*(05), 376–384. https://doi.org/10.2118/4142-PA

Wilkinson, M., & Haszeldine, R. S. (2002). Fibrous illite in oilfield sandstones—A nucleation kinetic theory of growth. *Terra Nova*, *14*(1), 56–60. https://doi.org/10.1046/j.1365-3121.2002.00388.x

Wilson, L., Wilson, M. J., Green, J., & Patey, I. (2014). The influence of clay mineralogy on formation damage in North Sea reservoir sandstones: A review with illustrative examples. *Earth-Science Reviews*, *134*, 70–80. https://doi.org/10.1016/j.earscirev.2014.03.005

Wong, T., & Brace, W. F. (1979). Thermal expansion of rocks: Some measurements at high pressure. *Tectonophysics*, *57*(2–4), 95–117. https://doi.org/10.1016/0040-1951(79)90143-4

Yasuhara, H., Kinoshita, N., Ohfuji, H., Takahashi, M., Ito, K., & Kishida, K. (2015). Long-term observation of permeability in sedimentary rocks under high-temperature and stress conditions and its interpretation mediated by microstructural investigations. *Water Resources Research*, *51*, 5425–5449. https://doi.org/10.1002/2014WR016427

You, Z., Bedrikovetsky, P., Badalyan, A., & Hand, M. (2015). Particle mobilization in porous media: Temperature effects on competing electrostatic and drag forces. *Geophysical Research Letters*, *42*, 2852–2860. https://doi.org/10.1002/2015GL063986

You, Z., Yang, Y., Badalyan, A., Bedrikovetsky, P., & Hand, M. (2016). Mathematical modelling of fines migration in geothermal reservoirs. *Geothermics*, *59*, 123–133. https://doi.org/10.1016/j.geothermics.2015.05.008

Yu, M., Hussain, F., Arns, J. Y., Bedrikovetsky, P., Genolet, L., Behr, A., et al. (2018). Imaging analysis of fines migration during water flow with salinity alteration. *Advances in Water Resources*, *121*, 150–161. https://doi.org/10.1016/j.advwatres.2018.08.006